Automation and Control of Fabry-Pérot Interferometers

Enrico Canuto
Politecnico di Torino
Dipartimento di Automatica e Informatica
Corso Duca degli Abruzzi 24
10129 Torino, Italy
enrico.canuto@polito.it

Fabio Musso, Luca Massotti
Politecnico di Torino and
Alenia Spazio, Strada Antica di Collegno 253
10146 Torino, Italy
fabio.musso@polito.it,
luca.massotti@polito.it

Abstract

Fabry-Pérot interferometry (FPI) originally invented for spectroscopy is now evolving as a basic technology for ultra-fine dimensional stabilization and measurement. To this end, the light path length of an optical cavity and the wavelength of a laser source injected into the cavity have to be each other tuned through a set of frequency and/or displacement actuators driven by a sharp and narrow signal encoding total cavity detuning. Digital control is essential in facilitating and automating the FPI use in view of space applications and routine instrumentation. Embedded model control (EMC) technology developed by one of the authors has been employed. Experimental results are presented.

1. Introduction

Fabry-Pérot interferometer (FPI) was invented by the French physicists Fabry and Pérot at the end of the XIX century (1899) to enable high resolution observation of spectral lines. Multiple light reflection between two plane surfaces create interference patterns which being very sensible to wavelength and optical path length were employed in the course of the XX century as scanning spectrometers. A significant improvement was made since 1970 by piezo-tuning the FPI optical length and in 1984 the 1st application to the measurement of small displacements took place. A further breakthrough came from their coupling with laser sources: first, the spectral line of a laser source can be measured and therefore controlled in purity and stability, second, the optical path length of a FPI can be tuned to a stable laser wavelength by a piezo-electric ceramics for revealing displacements of the order of 1 pm and less.

FPI made by vacuum cavities between two highly reflecting mirrors are employed for detecting gravitational waves in LIGO [10] and VIRGO [9] ground experiments and have been suggested as metrology lines for measuring and stabilizing linear/angular dimensions of space telescopes like GAIA [4]. Small vacuum cavities (long less than 20 cm), highly stable in length, are employed as frequency references having high spectral purity. Short-time (<10 s) length stability is achieved by ultra-low CTE glass like ULE©, stable vacuum thermal bath and suitable suspensions [7]. Frequency references of this kind are expected to be become a key technology for space interferometry (GAIA [4], LISA [14], Darwin), ground/space optical communications and time standards referenced to visible atomic transitions. One of the authors, contributing to this technology since 1997, implemented several digital control loops and automation to improve and facilitate FPI [3], [4], [5], [6].

PFI control problems and theirs solution to be mechanized into a Digital Control Unit (DCU) will be the subject of this paper. Section II will provide a brief illustration of FPI principles, applications and output signals to be fed back. Section III will present a unified treatment of the FPI automation and control problems assuming multiple actuation [5] and Embedded Model Control (EMC) technology [12], [13]. Section IV will present experimental results. Formulation will be free of theorem and proofs for sake of brevity and readability.

2. Fabry-Pérot interferometry

2.1. Basic principles and applications

Fabry-Pérot interferometers (FPI) treated in this paper are optical cavities [1] made by two aligned and highly reflecting mirrors where a laser light-wave is injected and a standing reflecting wave is created and kept either by regulating the incident wave frequency and/or by fine moving either mirror. As a result the cavity becomes an optical resonator as the injected light intensity is amplified inside the cavity under very low losses as in vacuum. Intensity amplification is measured by the *cavity finesse* $\mathcal{F}$ [1] which depending on mirror reflectivity can reach values greater than 10^5. Any

0-7803-9402-X/05/$20.00 © 2005 IEEE

frequency perturbation of the incident light-wave as well as any perturbation of the optical path inside cavity tends to destroy the standing reflecting wave (or resonant) condition by varying the intensity of the light-wave emitted by the cavity itself, which wave may be arranged to encode, scaled by cavity finesse, perturbation amplitude and sign.

Let $f_l = c/\lambda_l$ be the incident light frequency, typically 100 to 1000 THz (from near infrared to violet), related to wavelength λ_l by the speed of light in vacuum c. Then denote cavity length with L, typically 0.01 to 100 m, measured along the optical axis joining the spot centres of the laser beam on each mirror. The standing wave condition implies an integer ratio between length and wavelength

$$L = N\lambda_l/2 \Rightarrow f_l L = Nc/2,\ N \text{ integer}. \qquad (1)$$

A pair (f_l, L) satisfying the above condition is called a *resonant pair* and will be denoted as $(f_o(N), L_0(N))$. From (1), it is immediate that two successive resonant pairs indexed N, $N\pm1$ are separated in length by half-wavelength $\lambda_0/2$ and in frequency by the so-called *Free Spectral Range* (FSR)

$$F_0 = 0.5c/L_0 = 1/\tau_0, \qquad (2)$$

where τ_0 is the light travel time from mirror to mirror inside the cavity and $F_0 \simeq 150$ MHz @ $L_0 = 1$ m. It can be shown [8] that cavity dynamics in creating and destroying resonant conditions can be written as a 1st order discrete-time state equation having time unit τ_0 and time constant $\tau \simeq \mathfrak{F}\tau_0/\pi$, which for low finesses $\mathfrak{F} \le 500$ and $L_0 \le 1$ m, is less than 1 μs and will be neglected hereafter.

Actually, condition (1) can not be exactly met, but only approached, by forcing frequency and length to fluctuate around a resonant pair through active control. Thus by denoting length and frequency fluctuations (often called detuning) with $\Delta L = L - L_0(N)$ and $\Delta f = f_l - f_0(N)$ and fractional detuning with η, and by rewriting (1) as

$$(f_0 + \Delta f)(L_0 + \Delta L) = f_0 L_0 (1+\eta) \qquad (3)$$

a linear differential equation relating length and frequency detuning less the cavity detuning e can be written

$$\Delta f + (f_0/L_0)\Delta L = e,\ e = f_0\eta. \qquad (4)$$

The above relation, called *lock-in condition*, holds only under sufficiently small detuning e, where small is dictated by cavity finesse $\mathfrak{F}$.

Remark. Notice that although e must be kept very small (see (6)), the error components in (4), i.e. the length and frequency detuning ΔL and Δf, may be very large in comparison to e as far as each other compensate as in the tracking problem 3) below. Their limit is only dictated by length and frequency actuator range.

As the length-to-frequency scale $k_0 = f_0/L_0$ is usually much greater than 10^{12} and frequency detuning Δf can be accurately measured below 1 Hz, FPI may reveal sub-atomic length detuning, well below Bohr radius (50 pm). This is achieved by revealing e (encoded in the emitted light-wave) through a suitable opto-electronic chain named after Pound, Drever and Hall (PDH) [2] and by keeping e as small as possible through a control loop.

Accordingly, three main applications can be conceived:

1) *Length stabilization*: Δf is kept negligible by a frequency-stabilized laser source, which implies (4) to reduce to $\Delta L = L_0 e/f_0$ and to keep ΔL to zero by piezo-electric actuators (f.i. lead-zirconate-titanate/PZT ceramics) [3], [4].
2) *Frequency stabilization:* ΔL is kept negligible, for instance, by thermal control and ultra-low CTE (coefficient of thermal expansion) glass [7], which implies (4) to reduce to $\Delta f = e$. Then Δf is kept to zero by locking the incident laser frequency to cavity length by means of suitable frequency actuators (again PZT ceramics, thermal control) [5].
3) *Length measurement and tracking:* a frequency stabilized laser wave is detuned by a frequency actuator prior to be injected in the cavity so as to zero e in presence of a length detuning ΔL. The actuated Δf is made proportional to ΔL up to residual detuning e, laser frequency instability and actuator noise. The scale factor f_0/L_0 needs only to be calibrated for what concerns L_0 as f_0 is ensured by laser frequency stabilization. L_0 can be accurately measured by forcing frequency actuator to jump from current resonant condition N to $N\pm1$. As ΔL may be the result of artificial and natural causes, f.i. micro-thrusts as in [6], FPI can be made to reveal microscopic phenomena.

In all applications, cavity detuning e plays the role of the performance variable to be kept close to zero and below a predefined tolerance within a frequency bandwidth.

2.2. Response of PDH chain and FPI performance

According to Pound-Drever-Hall (PDH) technique [2], the cavity detuning e is encoded in the emitted light-wave as the amplitude and phase of a radio-frequency modulation (typically $f_m \le 0.1F_0$) applied to the incident laser beam and then revealed by demodulating the emitted light intensity collected by a photodiode. To dispose of a sharp zero-crossing at

resonant condition (1), the demodulated amplitude V of $\sin(2\pi f_m)$ is employed as the FPI measurement. The corresponding static response $V = h(e)$, frequency-to-voltage, is highly nonlinear (Figure 1) and periodic, the period being equal to FSR F_0.

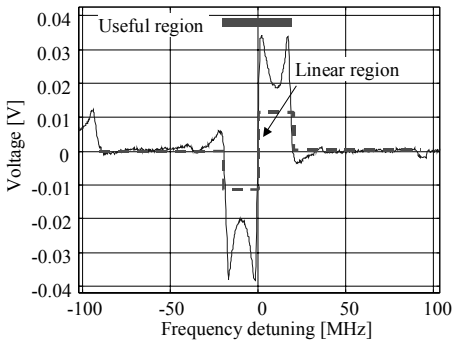


Figure 1 Typical response of the PDH chain versus frequency detuning.

For control purposes, the normalized response, frequency-to-frequency, is defined

$$H(e) = h(e)/k_{\max},\ k_{\max} = 2V_{\max}/e_{\max}, \qquad (5)$$

where $V_{\max}$ denotes the peak voltage before and after a zero crossing corresponding to a resonant condition and $e_{\max} \simeq 0.5F_0/\mathfrak{F}$ indicates the corresponding frequency detuning. Only in the *useful region*, centered on a zero crossing and large $2f_m$, $H(e)$ is different from zero and is a sector nonlinearity [15] of the kind $[0,1]$, i.e. it lies between the horizontal axis and the unitary slope line. In a smaller region, the *linear region* large $2e_{\max}$, it becomes monotonic, undergoes a sharp zero crossing suitable for regulation/tracking and holds

$$H(e) = k_{\max} e/\left(1+\left(e/e_{\max}\right)^2\right),\ |e/e_{\max}| \le 1. \qquad (6)$$

In this sub-region the sector nonlinearity is $[0.5,1]$.

The values of the application reported in [6], namely $L_0 = 0.195$ m and $\mathfrak{F} \cong 110$, yield a linear region width $e_{\max} \cong 3.5$ MHz, which for a laser frequency $f_l = 563$ THz (green light) corresponds to an upper bound $e_{L,\max} \simeq 1.2$ nm, if expressed in length units. The error e must be kept confined by FPI active control well below such bounds.

Neglecting PDH dynamics, the measurement y_f in frequency units, is related to e through the measurement error v and the response $H(e)$ as follows

$$y_f(t) = H(e) + v(t). \qquad (7)$$

By solving (7) for $e_L = e/k_0$, in length units, inside the linear region and making cavity finesse $\mathfrak{F}$ explicit yields

$$e_L(t) \simeq \lambda_0\left(y_f(t) - v(t)\right)/\left(4\mathfrak{F}e_{\max}\right),\ \lambda_0 = c/f_0 \qquad (8)$$

FPI performance depends on (8), namely:

1) $y_f(t)/e_{\max}$, the fractional control jitter, depends on the closed-loop control bandwidth and on the residual noise, usually due to mechanical vibrations.
2) $v(t)/e_{\max}$, the fractional PDH measurement error, depends on the PDH opto-electronics quality.
3) λ_0, from visible to near infrared, ranges from about $0.3\ \mu$m (violet) to $3\ \mu$m and depends on the application.
4) *Ceteris paribus,* e is attenuated by increasing $\mathfrak{F}$.

As an example, the space astrometry mission GAIA [4] asks for an average length detuning less than 1 pm (RMS) over a length $L_0 \simeq 1$ m, where the average must be taken over $\tau = 3$ s. Then by assuming infrared wavelength $\lambda_0 \simeq 1.3\ \mu$m and low finesse $\mathfrak{F} \simeq 150$, the target performance requires the average fractional jitter and PDH noise to be less than 0.1%, a standard target.

3. Unified automation and digital control formulation

3.1. FPI control tasks

With reference to (5) and (6), two tasks are needed:

1) *Lock-in detection and recovery (LDR)* detects the prolonged presence of e outside the useful range due to onset and shocks and returns it to linear range (Figure 2),
2) The *linear controller* operates under quasi-linear conditions, which are established as soon as e enters the linear range, i.e. $|e(t)| \le \bar{\eta} e_{\max}$, $\bar{\eta} < 1$.

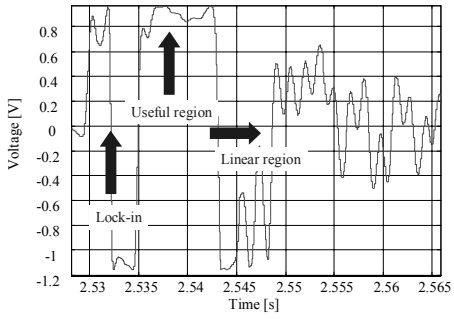


Figure 2 Arduous LDR of a suspended cavity ([6]) under severe length detuning due to pendulum beat ($> 3e_{\max}$/ms).

Actually, the linear controller may operate in a stable way also within the useful region (Figure 2), due to sector nonlinearity $[0,1]$, and it may be adjusted to improve stability when $|e(t)| \ge \bar{\eta} e_{\max}$. FPI may start to operate from arbitrary initial detuning $e(0)$ within the FSR F_0, very likely outside the useful region where the expected PDH signal is close to zero; which asks for lock-in detection.

Traditionally lock-in was kept through simple

analogue loops after lengthy, manual lock-in detection. Digital control and especially Embedded Model control are in favour of systematic automation and set-up as already discussed in [5] and [6].

3.2. Lock-in detection and recovery (LDR)

LDR is implemented by an hybrid closed-loop strategy based on a stylized shape of the PDH response, a doublet made as in Figure 1 by four parts corresponding to the values of the automaton state $\underline{a}$ (encircled capital letters in Figure 3):

1) unknown signal (DEFAULT),
2) zero or background signal (BACKGROUND),
3) signal inside extended region (SIGNAL),
4) zero crossing or linear region (LOCK-IN).

Control strategy has been designed so as to avoid false lock-in detection, which may occur due to parasitic zero-crossing, as well as to reduce lock-in detection time (in the order of seconds). The key strategy is a secure detection of the background signal, after which the extended region can be looked for. To this end, BACKGROUND state has been split into ZERO state, where background signal has to be confirmed, and SEARCH, where the extended region is looked for. Switching is driven either by time counter (doubly circled states in Figure 3) as from ZERO to SEARCH and/or by thresholds on PDH measure y_f. The output is the total commanded frequency $\underline{u}$ to actuators, whose rate may be modulated by automaton states. LOCK-IN triggers the linear controller. Escape from LOCK-IN is triggered by y_f and the model frequency detuning e (see below).

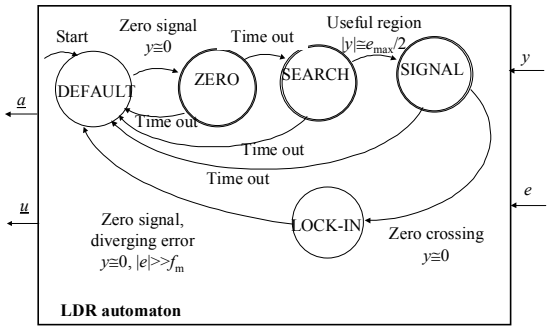


Figure 3 Essential diagram of the LDR state automaton.

3.3. Embedded model

The embedded model (EM) is the design model to be embedded as the core of the linear regulator. It is written as a discrete-time (DT) dynamics starting from (4) and (7), and by decomposing e as in [5] into a single disturbance $d_e(i)$ and multiple command components $c_j(i), j=1,...,m$, i being the generic discrete time. The underlying time unit T is the command sampling step to be designed ($T = 0.1$ ms in [5] and [6]). It results

$$\begin{aligned} e(i) &= d_e(i) + c(i),\ c(i) = \sum_{j=1}^{m} c_j(i) \\ y_e(i) &= H_m(e(i)) + v(i) \end{aligned}, \qquad (9)$$

H_m being an approximation of the true H, to be estimated and coded as a look-up table, while v accounts for PDH noise and aliasing errors due to sampling. Equation (9) must be completed with disturbance, actuator and sensor dynamics.

Disturbance dynamics model the disturbance class $\mathcal{D}$ which has to be rejected in order to guarantee target performance. As in [5], it is synthesized starting from the envelope of experimental/simulated PSD as the linear combination of white noise, random drifts and narrow-band noise tuned to specific frequencies. To guarantee robust observability, the corresponding DT dynamics has to be written as a series of elementary dynamics driven by 'arbitrary' DT signals $w_k(i)$ (they may be interpreted as DT white noise processes) to be collected into a vector $\mathbf{w}(i)$, as follows

$$\begin{aligned} d_e &= w_0 + \mathbf{D}\cdot\mathbf{w}_d = \\ &= w_0 + \mathbf{D}_1\cdot\left(w_1 + \mathbf{D}_2\cdot\left(w_2 + \cdots + \mathbf{D}_r\cdot w_r\right)\right) \end{aligned}, \qquad (10)$$

where $\mathbf{w}^T = \begin{bmatrix} w_0 & \mathbf{w}_d^T \end{bmatrix}$ and $\mathbf{D}\cdot\mathbf{w}_d$ denotes a linear DT operator acting on the causal sequence $\mathbf{w}_d = \{\mathbf{w}_d(i-k), k \geq 0\}$. The relevant Z-transform will be denoted by $\mathbf{D}(z)\mathbf{w}(z)$. The elementary dynamics $\mathbf{D}_k$ may assume two forms

$$\begin{aligned} \mathbf{D}^{(1)}(z) &= (z-1)^{-1} \\ \mathbf{D}^{(2)}(z) &= \alpha_k\left((z-1)^2 + \alpha_k(z-1) + \alpha_k\right)^{-1} \end{aligned} \qquad (11)$$

depending on drift or narrow-band assumption. F.i. the PSD in Figure 4 (upper plot, from [6]) has been modelled as

$$d_e = w_0 + \mathbf{D}^{(1)}\cdot\left(w_1 + \mathbf{D}^{(1)}\cdot\left(w_2 + \mathbf{D}^{(2)}\cdot w_3\right)\right), \qquad (12)$$

to include low-frequency drift and pendulum resonance.

The sequence of actuator dynamics $\mathbf{M}_j$ will be ordered as their low-frequency gains $b_j < \infty$, voltage-to-frequency: i.e. an increasing gain b_j from $j=1$ to m corresponds to a decreasing bandwidth α_j. The Z-transform of $\mathbf{M}_j$, assuming 1st order dynamics (2nd order may apply as in [11]), can be written as

$$c_j(z) = \mathbf{M}_j(z)u_j(z) = b_j\beta_j\left(z - 1 - \beta_j\right)^{-1}u_j(z), \qquad (13)$$

less actuator noise and modelling errors. The fastest actuator, $b_1 = \min_j\{b_j\}$, is assumed to be dynamic-free, i.e. $\beta_1 = 1$ in (13), and the resulting unit delay will be neglected.

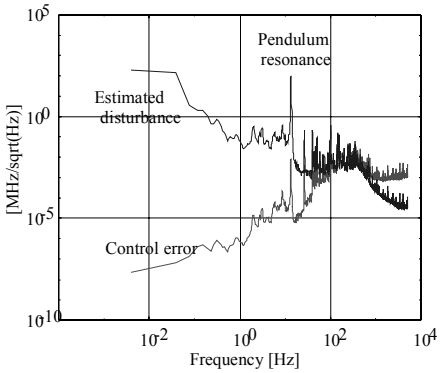


Figure 4 PSD of the estimated disturbance, from [6].

PDH dynamics can be usually neglected, but anti-aliasing filters have to be added in order to avoid spreading of wide-band disturbances (ground and acoustic noise) through feedback. Experience [4] and formal proof suggests a decimated 1st order digital anti-aliasing filter to be adopted. Denote with $T_y = T/N,\ N \geq 1$ the PDH sampling step and with k the corresponding discrete time. The anti-aliased PDH measure $y(i)$ holds

$$y(i+1) = y(i) + \sum_{h=k}^{k+N-1} y_f(k)/N \,. \qquad (14)$$

Among the advantages, the filter can be simply replicated into the EM as a DT integrator, thus avoiding unmodelled dynamics. It means that the EM output y_m is related to PDH output y_e, defined in (9), through the noise-free, BIBO unstable dynamics

$$y_m = \mathbf{M} \cdot y_e,\ \mathbf{M}(z) = (z-1)^{-1} \,. \qquad (15)$$

By restricting to PDH linear range (see Section 2.2), by employing the approximation $H_m(e) = e$ and defining a total disturbance d including the sum v of PDH noise and aliasing errors (the latter being very likely dominant) as $d = d_e + v$, the EM made by (9), (10), (13) and (15) can be written as

$$\begin{aligned} y_m &= \mathbf{M} \cdot \left(b_1 u_1 + \sum_{j=2}^{m} \mathbf{M}_j \cdot u_j + d \right) \\ d &= w_0 + \mathbf{D} \cdot \mathbf{w}_d + v \end{aligned} \,. \qquad (16)$$

The EM block-diagram is in Figure 5. A sequence of three actuators $j = 1,2,3$ from fastest to slowest have been included. Clouds denote the driving noise classes, usually interpreted as DT white noise. 2D boxes denote modelled dynamics (Z-transform). 3D boxes denote unmodelled dynamics (UD) in the form of a fractional dynamics driven by EM output variables. F.i. by restricting to the output $y(i)$ of the PDH chain and anti-aliasing filter, it will be related to y_m (see (15)) by

$$y = y_m + \Delta y = y_m + \partial\mathbf{P}(y_m, \mathbf{w}_e) \,, \qquad (0.17)$$

where $\partial\mathbf{P}(\cdot)$ denotes a DT dynamic operator, usually unknown and not realizable as a state equation, but driven by the causal sequence $y_m = \{y_m(i-k),\ k \geq 0\}$ less some other unknown input signals $\mathbf{w}_e$ independent on y_m and therefore on the EM commands. Each fractional UD $\partial\mathbf{P}(\cdot)$ can be given an analytic (linear) approximation $\partial\mathbf{P}(z;\mathbf{p})y_m(z)$ tunable by a parameter vector $\mathbf{p}$ to the elements of an uncertainty class.

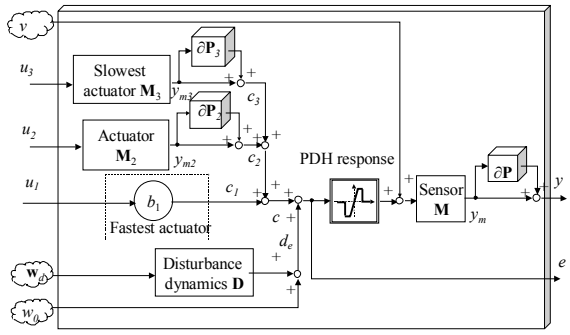


Figure 5 EM block-diagram.

3.4. Command law (CL)

As in [5], multiple commands will be exploited for apportioning disturbance rejection among different actuator capabilities. Denote with $\hat{d}$ an estimate of d provided by the Measurement Law (see below) and denote with $\hat{d}_j$ the portion to be tracked by actuator j subject to constraint $\hat{d}_m = \hat{d}$. Any actuator j will only track the low-frequency components of $\hat{d}_j$ defined by a low-pass filter, the *tracking dynamics*, to be designed and denoted by $\mathbf{V}_j$. As a consequence the following signal chain builds up

$$\begin{aligned} &\hat{d}_m = \hat{d} \\ &\hat{d}_{j-1} = (\mathbf{I} - \mathbf{V}_j) \cdot \hat{d}_j,\ j = m,...,2,\ \mathbf{S}_j = \mathbf{I} - \mathbf{V}_j \end{aligned} \,, \qquad (18)$$

where $\mathbf{S}_j$ is the sensitivity proper to $\mathbf{V}_j$. To match actuator capabilities (gain and bandwidth), the sequence of sensitivities $\{\mathbf{S}_m,\ldots,\mathbf{S}_2\}$ will be designed to have increasing bandwidth as in [5]. This is done by appropriate tuning the eigenvalue set Λ_j of $\mathbf{V}_j$.

Tracking dynamics is designed as a dynamic input-output feedback $\mathbf{H}_j$ around the actuator model $\mathbf{M}_j$, where $\mathbf{H}_j$ must include a DT integrator to allow perfect tracking of dc components. F.i. in the 1st order case as in (13), the simplest feedback can be shown to hold

$$\mathbf{H}_j(z) = (z-1)^{-1}\left(h_{0j} + h_{1j}\left(z - 1 - \gamma_j\right)^{-1} \right). \qquad (19)$$

It gives rise to a 3rd order low-pass filter $\mathbf{V}_j$ whose gains $\{\gamma_j, h_{0j}, h_{1j}\}$ are easily computed from the assigned Λ_j. Higher orders models $\mathbf{M}_j$, asking for more complex design of $\mathbf{H}_j$, will not be treated here.

The chain (18) has to be completed with the command

apportionment equation

$$u_j = \underline{u}_j - \mathbf{H}_j \cdot \mathbf{S}_j \cdot \hat{d}_j = \underline{u}_j - \mathbf{H}_j \cdot \hat{d}_{j-1},\ j = m,...,2 \quad (20)$$

the negative sign forcing disturbance rejection and $\underline{u}_j$ being the command computed by LDR (see Section 3.2), if the case.

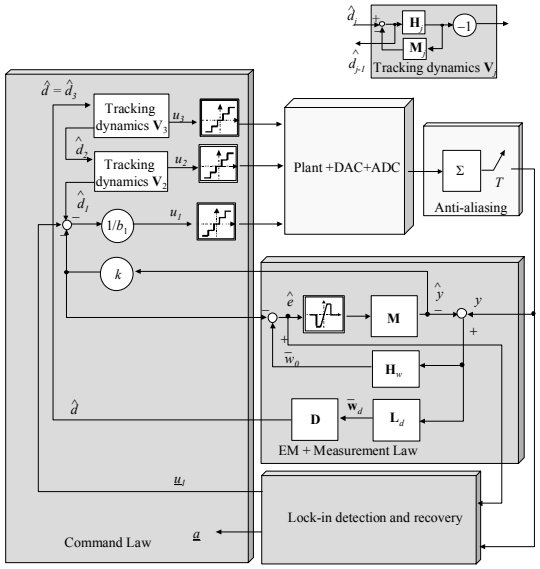


Figure 6 Block-diagram of CL and ML.

The fastest actuator (see [5]) must complete disturbance rejection with internal stability properties. To this end, it must force the effects of the bounded residual disturbance

$$\hat{e}_d = d - \hat{d} \quad (21)$$

to be bounded all over the feedback chain. This is achieved by stabilizing the anti-aliasing filter (15) through state feedback so as to avoid $\hat{e}_d$ integration into drift. Owing to 1st order in (15), the scalar feedback $c_{CL} = -k\hat{y}$, in frequency units, from the model output estimate $\hat{y}$ (see Section 3.5) is sufficient to the purpose, thus bringing to the command law

$$u_1 = \underline{u}_1 - \left(k\hat{y} + \hat{d}_1\right)/b_1 . \quad (22)$$

The complete CL is made by (18), (20) and (22). CL mechanization in the DCU has to be completed by command digitization providing the digital command vector $\tilde{\mathbf{u}}(i)$ to plant DAC. Figure 6 shows the block-diagram of the command and measurement laws. The DT integrator of the anti-aliasing filter is denoted through a boxed Σ and sampling symbol.

3.5. Measurement Law (ML)

Define the model error (or output innovation)

$$\hat{e}_y(i) = y(i) - \hat{y}(i) \quad (23)$$

as the discrepancy between the anti-aliased, decimated, PD measure y in (14) and the estimate $\hat{y}$ of the model output y_m in (16). The ML aims at estimating the driving noise $\mathbf{w}(i)$ of the class $\mathcal{D}$ under causality constraints. First, only a causal estimate $\bar{\mathbf{w}}(i)$ depending on $\hat{e}_y(i)$ and therefore correlated to past occurrences $\mathbf{w}(i-k)$, $k > 0$ can be obtained, which, since Kalman filter, has been shown to be sufficient for updating $\hat{d}$ and guaranteeing the residual $\hat{e}_d$ in (21) to be (statistically) bounded. Second, $\hat{d}(i)$ must be estimated as a one-step prediction $\hat{d}(i) = \hat{d}(i/\bar{\mathbf{w}}(i-1))$ to allow CL mechanization one-step in advance, which implies $\hat{d}$ only to depend on the strictly causal part in (10):

$$\hat{d}(z) = \mathbf{D}(z)\bar{\mathbf{w}}_d(z) . \quad (24)$$

This entails ML to separate into a pair of feedback laws around EM (16) and driven by $\hat{e}_y$ as follows.

1) The dynamic feedback to predictable disturbance

$$\hat{d}(z) = \mathbf{D}(z)\bar{\mathbf{w}}_d(z) = \mathbf{D}(z)\mathbf{L}_d(z)\hat{e}_y(z) = \mathbf{H}_d(z)\hat{e}_y(z) \quad (25)$$

2) The dynamic feedback to unpredictable noise

$$\bar{w}_0(z) = \mathbf{H}_w\hat{e}_y(z) . \quad (26)$$

Then, model output $\hat{y}$, model error $\hat{e}_y$ and residual disturbance $\hat{e}_d$ can be expressed by

$$\begin{aligned} \hat{e}_y &= \mathbf{S}_w \cdot \left(y - \mathbf{M} \cdot u_{CL}\right) = \mathbf{S}_w \cdot \mathbf{M} \cdot \hat{e}_d \\ \hat{e}_d &= d - \hat{d} = \mathbf{S}_d \cdot d,\ \hat{y} = y - \hat{e}_y \end{aligned}, \quad (27)$$

upon definition of a pair of sensitivity operators

$$\begin{aligned} \mathbf{S}_w &= \left(I + \mathbf{H}_w \cdot \mathbf{M}\right)^{-1} \\ \mathbf{S}_d &= \left(I + \mathbf{H}_d \cdot \mathbf{S}_0 \cdot \mathbf{M}\right)^{-1} \end{aligned}, \quad (28)$$

which in turn combine into the overall ML sensitivity

$$\mathbf{S}_{ML} = \mathbf{S}_w \cdot \mathbf{S}_d = \left(I + \left(\mathbf{H}_w + \mathbf{H}_d\right) \cdot \mathbf{M}\right)^{-1} . \quad (29)$$

It can be shown from (18), (20) and (22) that the embedded model (16) can be mechanized in the DCU as

$$\hat{y} = \mathbf{M} \cdot \left(c_{CL} + \mathbf{H}_w \cdot \hat{e}_y\right) . \quad (30)$$

Then (30) and the feedback laws (25) and (26) constitute a state predictor driven by c_{CL} and $\hat{e}_y$. The gains of the feedback laws encoded in $\mathbf{H}_w$ and $\mathbf{L}_d$ are tuned by assigning the eigenvalue set Λ_{ML} of the prdictor complementary sensitivity $\mathbf{V}_{ML} = I - \mathbf{S}_{ML}$. As the anti-aliased measure $y(i)$ is noise-free, eigenvalue tuning will be only constrained by unmodelled dynamics (see Section 3.7) and not by measurement noise as in Kalman filter design.

3.6. Average performance

Let $\underline{e}(i)$ be the sampled average of the performance variable $e(t)$ over $T = NT_y$, where T_y is the sampling

time defined in Section 3.3. From (9), (16) and the definition of d, it follows

$$\begin{aligned}\underline{e}(i) &= b_1 u_1(i) + \sum_{j=2}^{m} \left(\mathbf{M}_j \cdot u_j\right)(i) + \underline{d}(i) - \underline{v}(i) \\ \underline{e}(i) &= -k\hat{y}(i) + \underline{\hat{e}}_d(i) - \underline{v}(i)\end{aligned}, \quad (31)$$

where $\underline{\hat{e}}_d(i) = \underline{d}(i) - \hat{d}(i)$. Then by introducing the command law feedback operator

$$\mathbf{V}_{CL} = \left(I + k\mathbf{M}\right)^{-1} k\mathbf{M} = k(z - 1 - k)^{-1} \quad (32)$$

one obtains

$$\underline{e} = -\underline{v} + \left(I - \mathbf{V}_{CL} \cdot \mathbf{M}^{-1} \cdot \left(I - \mathbf{S}_w\right) \cdot \mathbf{M}\right) \cdot \mathbf{S}_d \cdot \underline{d} \quad (33)$$

which in the SISO case and assuming $\mathbf{V}_{CL} \simeq I$ simplifies to

$$\underline{e} \simeq -\underline{v} + \mathbf{S}_{ML} \cdot \underline{d}\,. \quad (34)$$

Finally, by reusing definition $d = d_e + v$, one obtains the classical equation

$$\underline{e} \simeq -\mathbf{V}_{SM} \cdot \underline{v} + \mathbf{S}_{SM} \cdot \underline{d}_e\,, \quad (35)$$

where $\underline{v}(i)$ and $\underline{d}_e(i)$ are practically aliasing-free, being the time average of $v(t)$ and $d_e(t)$. Equation (35) shows performance to be limited by low-frequency components of $\underline{v}$, which may be affected by non-stationary components like flicker noise (PDH electronics), and by the bandwidth of $\mathbf{V}_{ML}$.

3.7. Robust stability versus unmodelled dynamics

Performance and stability are affected by unmodelled dynamics $\partial\mathbf{P}(\cdot)$, not explicitly formulated for sake of brevity (see Figure 5). F.i. residual disturbance $\hat{e}_d$ may be affected by an oversimplified dynamics $\mathbf{M}_j$ in the frequency region close to control rate $f_c = 1/T$. In which case, internal stability is no more guaranteed by (22), as $\hat{e}_d$, now command dependent, creates a new closed-loop which is out-of-design and, worse, uncertain. Stability and performance are recovered as in [5], by constraining the eigenvalues of the tracking dynamics $\mathbf{V}_j$ and of the predictor sensitivity $\mathbf{S}_{ML}$ to free $\hat{e}_d$ from the unmodelled dynamics effects below a certain threshold. This is first obtained through analytic approximations of the unmodelled dynamics and then refined through simulated experiments and field tests. Of course, eigenvalue constraints will restrict the bandwidth of $\mathbf{V}_j$ and $\mathbf{V}_{ML}$, thus degrading disturbance rejection. Degradation may be overcome by careful disturbance modelling close to such band limits.

4. Experimental and simulated results

Experimental results refer to

1) a ground test-bed to demonstrate FPI in the sub-nanometric dimensional stabilization (in vacuum) of space optics with mass >1 kg and size ≥ 1 m [3], [4],
2) digital frequency stabilization of a monolithic laser source through a set of coordinated actuators (acousto-optic modulator, PZT ceramics, thermal control) [5],
3) an instrument for space micro-thruster qualification, where the laser source frequency is actuated by PZT ceramics and thermal control to track and measure the length detuning of a Fabry-Pérot cavity due to micro-thruster force [6]. (see Figure 7).

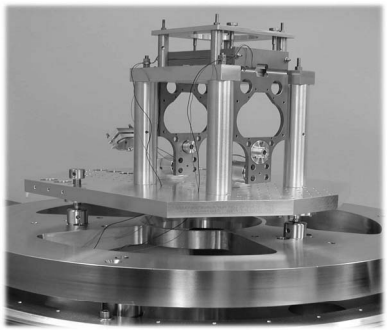


Figure 7 Thrust-stand [6] without vacuum cover.

Simulated results refer to the ground breadboard of a metrology line, now under construction, for measuring and possibly stabilizing thermo-elastic deformations of the GAIA telescope [4]. Metrology lines are a development from the test-bed mentioned in [3]. A stabilized laser frequency is detuned by an acousto-optic modulator to track and measure the length detuning of a cavity mounted on the optics.

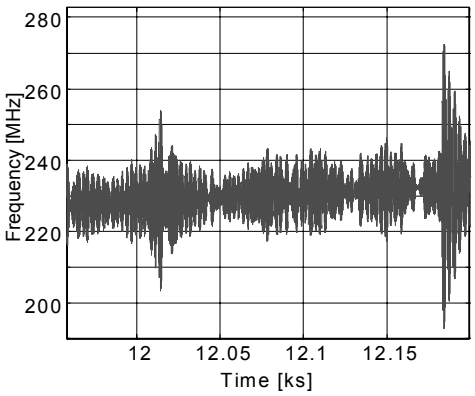


Figure 8 Raw frequency measures affected by 13 Hz pendulum beat.

Figure 4 shows the PSD of the estimated length

detuning (upper plot) of the cavity under zero force, corresponding to the sum of instrument and laser source noise. The lower plot is the control jitter PSD showing tracking of length detuning up to 100 Hz, so as to include the parasitic pendulum resonance at 13 Hz for calibration. Actually the parasitic resonance, due instrument imbalance and ground noise, affects the length measurements but it can be filtered for revealing length measures up to 2 Hz with a resolution better than 1 μN , as Figure 8 and Figure 9 show (see also [6]).

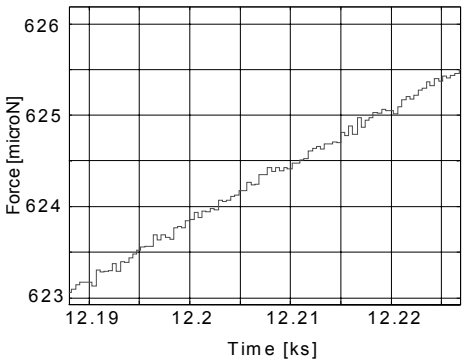


Figure 9 Filtered force measures revealing μN drift.

Experimental results showing command apportionment can be found in [5] and [11]. Figure 10 shows command apportionment for the suspended cavity of the micro-thruster instrument where a voice coil has been added to laser PZT and thermal control to suppress parasitic resonance at 13 Hz (see Figure 4). As pointed out in [5], although a single command rate, $f_c = 10$ kHz , is adopted for all commands to simplify mechanization, multi-rate actuation naturally results due to progressive bandwidth restriction and resolution relaxation from faster to slower actuators.

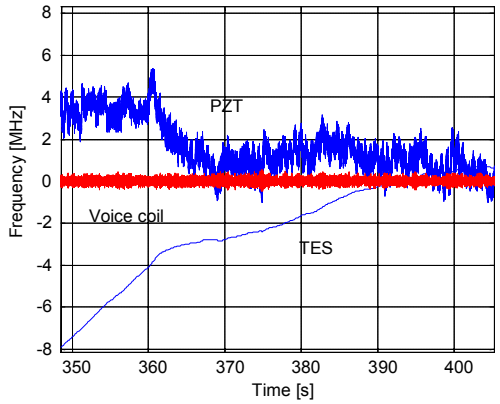


Figure 10 Command apportionment from [11].

Acknowledgments

This work was in part supported by grants from Alenia Spazio, Torino, Italy, within research projects sponsored by European Space Agency.

Abbreviations

DT discrete time, EM embedded model, PSD power spectral density, FPI Fabry-Pérot interferometer, ML measurement law, CL command law, DCU digital control unit, PDH Pound-Drever-Hall, LDR lock-in detection and recovery, FSR free spectral range, UD unmodelled dynamics.

References

[1] A.E. Siegman, *Lasers,* Sausalito (CA): Univ. Science Books, 1986.

[2] R. W. Drever, J.L. Hall, F.W. Kowalski, J. Hough, G.M. Ford, A.J. Munley *et al*., "Laser phase and frequency stabilization using an optical resonator", *Appl. Phys. B*, 1983, 21, 97-105.

[3] F. Bertinetto and E. Canuto, "Sub-nanometer digital positioning of large bodies by Fabry-Pérot interferometry", *Opt. Eng.,* 40 (1), 2001, 76-80.

[4] E. Canuto "Sub-nanometric optics stabilization in view of the GAIA astrometric mission", *Control Eng. Practice,* 11 (5), 2003, 569-578.

[5] E. Canuto and A. Rolino "Multi-input digital frequency stabilization of monolithic lasers", *Automatica*, 40(12), 2004, 2139-2147.

[6] E. Canuto and A. Rolino "An automated interferometric balance for micro-thrust measurement", *ISA Trans.*, 43(2), 2004, 169-187.

[7] S.A. Webster, M. Oxborrow and P. Gill, "Subhertz-linewidth Nd:YAG laser", *Opt. Lett.,* 29, 1497, 2004.

[8] D. Redding, M. Regehr and L. Sievers "Dynamic models of Fabry-Pérot interferometers", *Applied Optics,* 41 (15), may 2002, 2894-2906.

[9] B. Caron, A. Dominjon, F. Marion, L. Massonnet, D. Morand, B. Mours *et al*. "Status of the VIRGO experiment". *Nucl. Instrum. Meth.* 360, 1995, 258-262.

[10] A. Abramovici, Althouse, J. Camp, D. Durance, J. A. Giaime, A. Gillespie *et al.* "Improved sensitivity in a gravitational wave interferometer and implications for LIGO". *Physics Letters A* 218(8), 1996, 157-163.

[11] E. Canuto and A. Rolino, "Active vibration suppression in a suspended Fabry-Pérot cavity", in *Proc. 2004 American Control Conf.,* Boston (MA, USA), June 30-July 2, 3660-3665.

[12] E. Canuto, F. Musso and D. Andreis "Embedded Model Control: application to electro-valves", accepted to *13th Mediterranean Conference on Control and Automation*, Limassol (Cyprus), June 27-29, 2005..

[13] E. Canuto Controlli Automatici, Parte II. Controllo digitale. Turin (Italy), CELID, 2002 (in Italian).

[14] LISA Web Page: http://sci.esa.int/science-e/www/area/index.cfm?fareaid=27.

[15] M. Vidyasagar *Nonlinear Systems Analysis,* Englewood Cliffs (NJ), Prentice-Hall, Inc., 1987.